The evolution of a breaking mesospheric bore wave packet

R. G. Stockwell,[1] M. J. Taylor,[2] K. Nielsen,[2] and M. J. Jarvis[3]

[1] All-sky CCD observations of mesospheric gravity waves have been made from Halley Station Antarctica (75.5°S, 26.7°W) as part of a collaborative research program between British Antarctic Survey, U.K. and Utah State University, USA. A mesospheric bore event was observed in the nightglow emissions over a period of several hours on the 27th of May, 2001. Two dimensional S-Transform (ST) analysis is applied to the airglow images of this bore event. This local spectral technique allows one to calculate the wave parameters as a function of time and space. It is observed that the horizontal phase speed and wavelength decrease over time as the amplitude attenuates. Simultaneously with this wave event the background wind experiences a large acceleration in the direction of the wave propagation. Mesospheric bore theory calculations are used to estimate the bore duct depth and it is shown that as the wave packet evolves, the bore duct collapses (decreasing in its vertical extent). As the bore duct shrinks, the wave's group velocity decelerates, the amplitude attenuates, and the wave dissipates.

Citation: Stockwell, R. G., M. J. Taylor, K. Nielsen, and M. J. Jarvis (2011), The evolution of a breaking mesospheric bore wave packet, *J. Geophys. Res.*, *116*, D19102, doi:10.1029/2010JD015321.

1. Introduction

[2] Passive imaging of airglow layers has provided many observations of spectacular two dimensional front events, many of which have been identified as mesospheric bores. The events are characterized as a step function change in observed intensity propagating through the field of view, often accompanied by a set of phase locked wavefronts.

[3] *Dewan and Picard* [1998] first outlined the basic theory for mesospheric bores based on hydraulic theory, calculating relationships between the vertical depth of the bore duct and bore jump height, and propagation speed, horizontal wavelength, and amplitude. In addition they also calculated energy dissipation rates and the rate of creation of bore wavefronts. Later work by *Seyler* [2005] applied the Navier-Stokes equations to model internal waves and nonlinear bores. More recently, *Laughman et al.* [2009] performed numerical simulations of nonlinear incompressible dynamics to explore bore generation and morphology for idealized thermal ducts, an idealized Doppler duct, and a combination of thermal and Doppler ducts at nearby altitudes.

[4] Observations of the bore characteristics, in both speed of the bore, and the wavelength of the phase locked waves have shown consistency. *Taylor et al.* [1995] first reported observations of what was later described as a undular mesospheric bore. *Batista et al.* [2002] observed a wall

event at Cachoeira Paulista (CP) (23°S, 45°W) in July 1999 that moved at 70 m s^{-1}. *Brown et al.* [2004] observed frontal structures in OH and OI airglow emissions over South Carolina, on the night of 14–15 October 2001. Four frontal events were reported, each with a speed in the range of 70 m s^{-1} though one had a high speed of 105 m s^{-1}. Due to a lack of a sharp defining structure, they did not regard these fronts as "wall events". *Smith et al.* [2003] observed a bore over the United States on November 14, 1999 with three spaced imagers as well as a lidar and meteor radar. These measurements indicated the presence of a strong vertical wind shear and a large temperature inversion. *She et al.* [2004] observed the transition of an undular bore into a foaming internal bore over Fort Collins in October 2002. Lidar measurements indicated the presence of a thermal duct. *Smith et al.* [2005] reported the formation of a mesospheric bore from a breaking gravity wave at Arecibo in May 2003 where a temperature inversion was observed in lidar measurements. *Medeiros et al.* [2005] recorded 64 bore events between September 2000 and September 2002 at Cariri, Brazil; the majority of these events were consistent with 70 m s^{-1} speeds and 20 km wavelengths. *Fechine et al.* [2009] observed an undular bore in a Doppler duct in October 2005 in Brazil. This bore had a wavelength of 42 km and a speed of 68 m s^{-1}. *Shiokawa et al.* [2006] observed a front-like structure at Kototabang, Indonesia. They reported a decrease in intensity of all airglow layers (OH, OI, O2 and Na) with the passage of the front. A thermal duct was observed in SABER data. *Yue et al.* [2010] observed 7 mesospheric bores over a 5 year period, each of them associated with large cold front systems in the troposphere. Common features reported in these observations were phase speeds of approximately 70 m s^{-1} and wavelengths of approximately 20 km. In our analysis similar

---

[1]Colorado Research Associates, Boulder, Colorado, USA.
[2]Center for Atmospheric and Space Sciences and Department of Physics, Utah State University, Logan, Utah, USA.
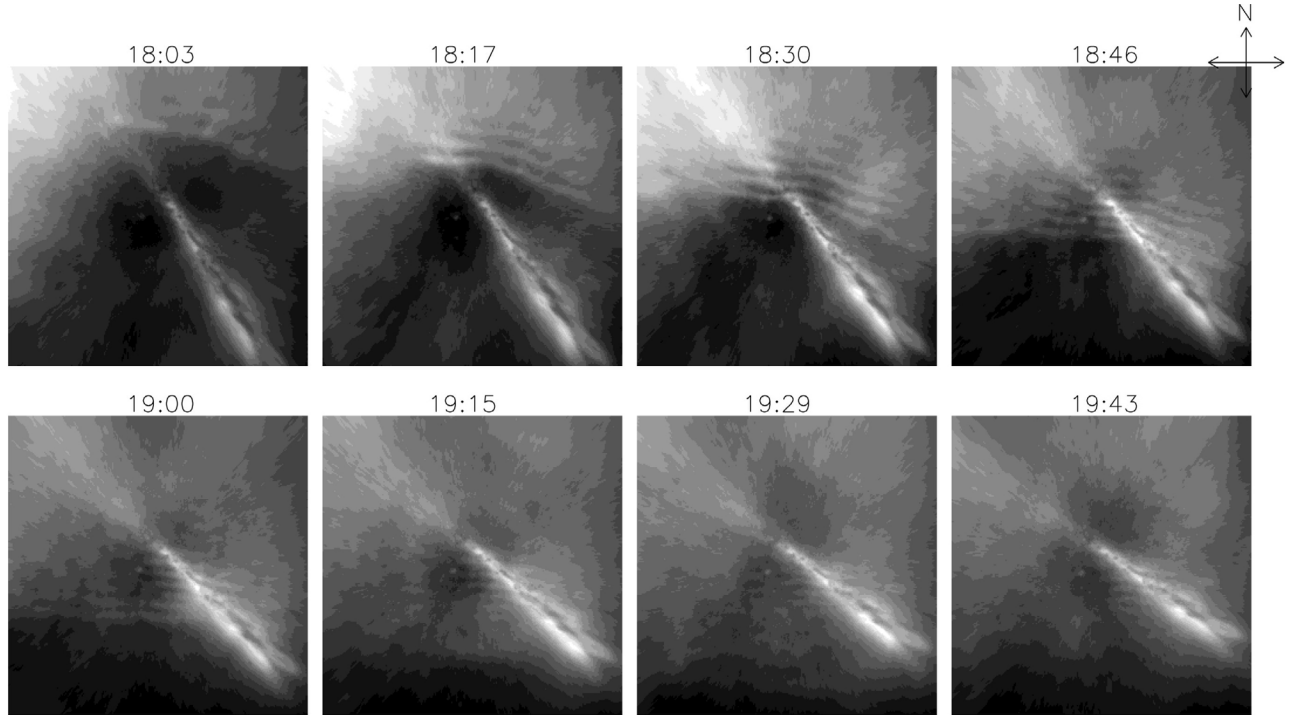[3]British Antarctic Survey, Cambridge, UK.

Figure 1. Eight images of the OH nightglow showing the unusual bore event. A very large wavefront is seen to move in from the north (top) of the images.

aggregate characteristic values are found, however the local spectral analysis technique employed here has the capability to probe the characteristics of the wave phenomena as a function of space and time, rather than give only an aggregate measure of the event. In doing so, the time and space evolution of the bore is captured and detailed observations of the bore duct are revealed.

2. Data Analysis

[5] Vertical wind profiles were measured by the BAS Imaging Doppler Interferometer (IDI) located at Halley Station, Antarctica (75.5 S, 26.7 W), along with all-sky CCD observations of the OH nightglow. The OH image data analyzed here consists of a series of near infrared images taken every 2 minutes over the night of May 27, 2001. The images have been photometrically flat fielded in order to correct for the difference of sensitivity of the pixels and the vignetting due to the optical system. Then, they were calibrated using the known star background to know the camera orientation, and projected onto a regular 500 by 500 km spatial grid (sampled at 0.98 km) using an assumed peak altitude of 87 km, to correct for the all-sky lens format. A large amplitude wave event is clearly evident propagating from the northern edge of the field of view as shown in Figure 1. Here, eight images are shown over a two hour period.

[6] To reduce Milky Way contamination of the signal, a high pass filter is applied temporally to each pixel of the data set. This is an effective technique as the Milky Way moves slowly through the field of view, much slower than the gravity waves analyzed in this report. In the operation

of the imager for this night, some breaks for calibration occur in the time series. These calibration breaks do not pose any problem whatsoever for the two dimensional spatial S-Transform gravity wave analysis used below, however regular sampling in time is required for temporal filtering. For this process, interpolated images were inserted into the time series at the calibration break, the temporal filter was applied, then these interpolated images were again removed from the result.

[7] Each image of the data was spatially (x, y) bandpass filtered with a second order Butterworth filter with a low wave number cut-off at 0.01 km^{-1} (corresponding to a 100 km wavelength) and a high wave number cut-off at 0.5 km^{-1} (corresponding to a 2 km wavelength). The cut-off wave number is the point for which the output of the filter is -3 dB of the nominal passband value. The time series from each pixel had a temporal high pass filter applied with a lower cutoff frequency of 0.00125 Hz (corresponding to a 13.3 min period almost a factor of three greater than the period of the observed wave). The temporal filtering function is performed as a time domain convolution of the data with a 3 point measurement length, which results in contamination of the 5 points surrounding the gap. Because the time offset is not uniform during these gaps, there is a phase discontinuity present in the filtered results, and therefore points where this contamination is present are excluded from the analysis.

[8] The result of the application of the filter is shown in Figure 2. In Figure 2a, the raw (flat fielded) OH airglow image is presented (same as the 18:17 UT image shown in Figure 1). Evident are the bright Milky Way signal
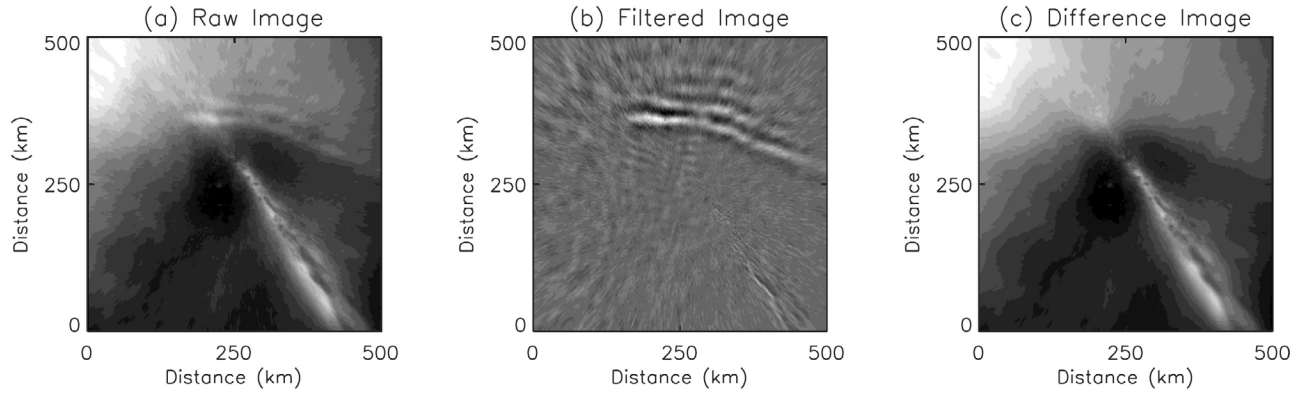
Figure 2. Illustration of the filtering effect and its enhancement of the wavefront. (a) Raw image at 18:17 UT. (b) Filtered image. (c) Residual image.

(a diagonal from bottom right to top left), and the bore event (wave features at the north edge of the image). Figure 2b, the filtered data with the Milky Way signal removed are shown. The bore wave signal is in the passband of the filter, and is unmodified by the preprocessing algorithm. However, the bore step (i.e. the increase in brightness that is phase locked to the wave packet) is also attenuated in the filtered data as evident in the residual (raw minus filtered) image shown in Figure 2c. The large increase in background intensity indicates the step function increase of OH brightness associated with a bore event.

2.1. Two Dimensional Local Spectral Analysis

[9] The S-Transform (ST) has been used extensively in the literature in its one dimensional form, but can be easily extended to higher dimensions. Details of the two dimensional S-Transform are given by *Mansinha et al.* [1997]. The discrete Fourier Transform of a function $h[kT]$ where the time index $k = 0, \ldots, N - 1$ and T is the sampling interval is given by *Brigham* [1974]:

$$H\left[\frac{n}{NT}\right] = \frac{1}{N}\sum_{k=0}^{N-1} h[kT]e^{-\frac{i2\pi nk}{N}} \qquad (1)$$

where the frequency index $n = 0,1,\ldots, N - 1$.

[10] The discrete 2-D S-Transform of an image $h[pTx, qTy]$ (where $p = 0,\ldots, N - 1$ and T_x is the sampling interval in the p direction, and $q = 0,\ldots, M - 1$ and T_y is the sampling interval in the q direction) is given by:

$$S\left(pT_x, qT_y, \frac{n}{NT_x}, \frac{m}{MT_y}\right)$$
$$= \sum_{n'=-N/2}^{N/2-1}\sum_{m'=-M/2}^{M/2-1} H\left(\frac{n'+n}{NT_x}, \frac{m'+m}{MT_y}\right)e^{-\frac{2\pi^2 n'^2}{n^2}}e^{\frac{i2\pi n'p}{N}}e^{-\frac{2\pi^2 m'^2}{m^2}}e^{\frac{i2\pi m'q}{M}} \qquad (2)$$

(For $n \neq 0$ and $m \neq 0$). For brevity, N and M are assumed even.

[11] In this analysis, the two dimensional spatial S-Transform is applied to each image. The two dimensional spatial ST transforms the image (x, y) at a given time t_0 into a 4-dimensional local spectral representation (x, y, k_x, k_y) at

that specific time t_0. The S-Transform is performed on each image giving us a five dimensional data set,

$$S[x, y, k_x, k_y, t] \qquad (3)$$

A typical nighttime measurement of airglow intensity data is comprised of a $1024 \times 1024 \times 200$ point data set $d[x, y, t]$. The spatial size has been downsampled by a factor of four (approximately a 2 km sampling interval) and three overlapping regions of 128 by 128 spatial samples have been utilized for practical computational reasons.

2.2. Cross ST Analysis: Wave Parameter Calculations

[12] A spatially local (i.e. near a spatial position x_0, y_0) quasi-monochromatic wave packet is represented as a peak in the local amplitude spectrum at a specific k_{x0}, k_{y0} from which the wave number of the wave can be directly read. A generalized instantaneous wave vector calculation can be used to interpolate the local spectrum and find the peak
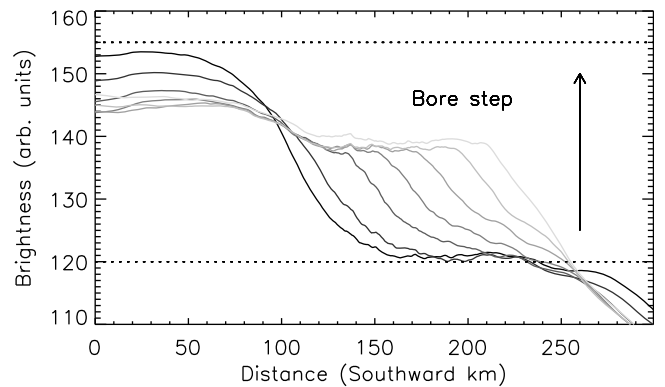

Figure 3. A plot of the east-west row average of the low-pass filtered images (Difference Images in Figure 2) where the bore waveform has been removed. The step function in OH brightness is apparent in these images, moving southward through the images at approximately 65 m s^{-1} (roughly the same speed as the bore wavefront). These traces are drawn for the times 18:19, 18:26, 18:36, 18:44, 18:52, 19:00, and 19:08 UT.
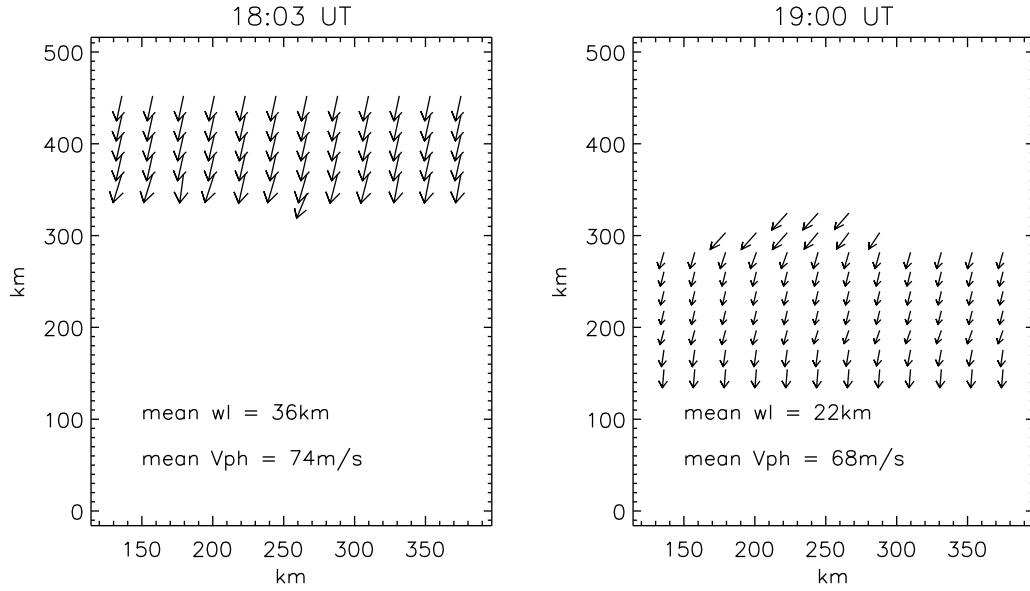
Figure 4. The horizontal wavelength for the bore wave packet for two different times. As the wave evolved, the wavelengths grow smaller, from a mean wavelength of 36 km at 18:03 UT with a phase speed of 74 m s^{-1} to a mean wavelength of 22 m s^{-1} at 19:00 UT with a phase speed of 68 m s^{-1}. The arrows are plotted in data coordinates, and the length of the arrow can be measured from the y-axis.

values with high resolution. The spatial phase shift of this particular wave (k_{x0}, k_{y0}) can be read from the phase difference at this peak between the S-Transforms of two successive images (t_0, t_1).

[13] The S-transform Shift Theorem states that if a time series $h(t)$ has an S-Transform $S(\tau, f)$

$$h(t) \Leftrightarrow S(\tau, f) \qquad (4)$$

then a translation in time of r leads to the following result:

$$h(t - r) \Leftrightarrow S(\tau - r, f)e^{-i2\pi fr} \qquad (5)$$

Thus cross spectral S-Transform analysis can be used to directly measure the spatial phase difference. More details on ST properties can be found in the work by *Stockwell*
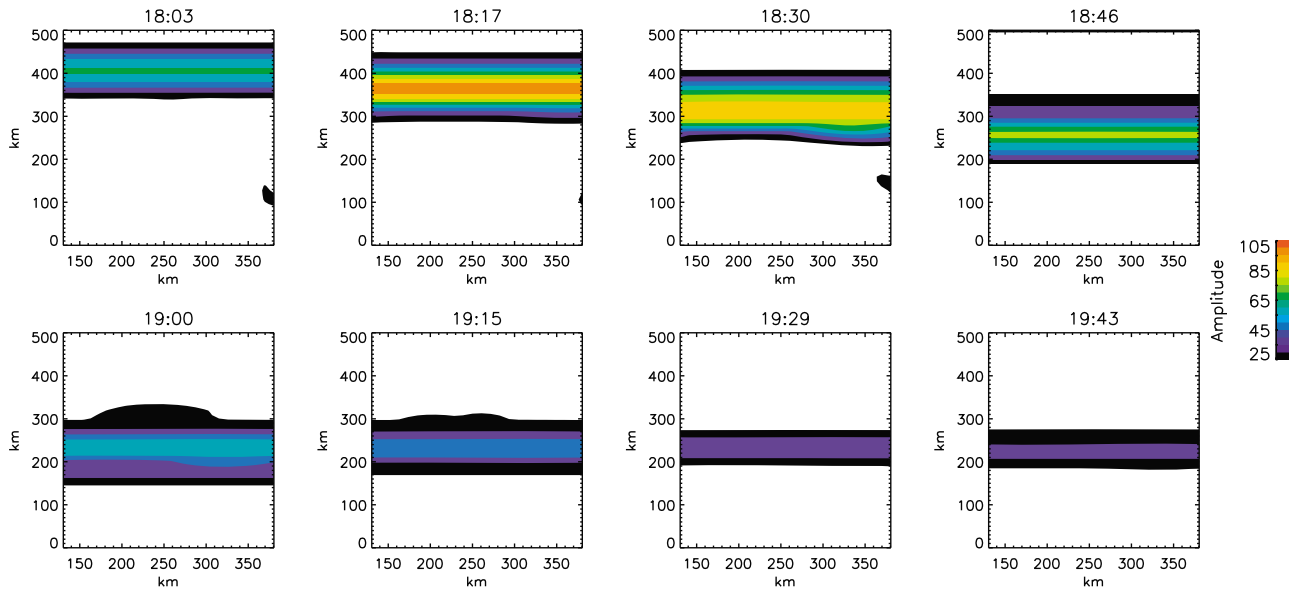

Figure 5. The wave amplitude for the bore wave packet for the same times as shown in Figure 1. The motion of the wave packet toward the top of the images indicates the group velocity of the wave packet which is consistent with the motion of the brightness step function shown in Figure 3.
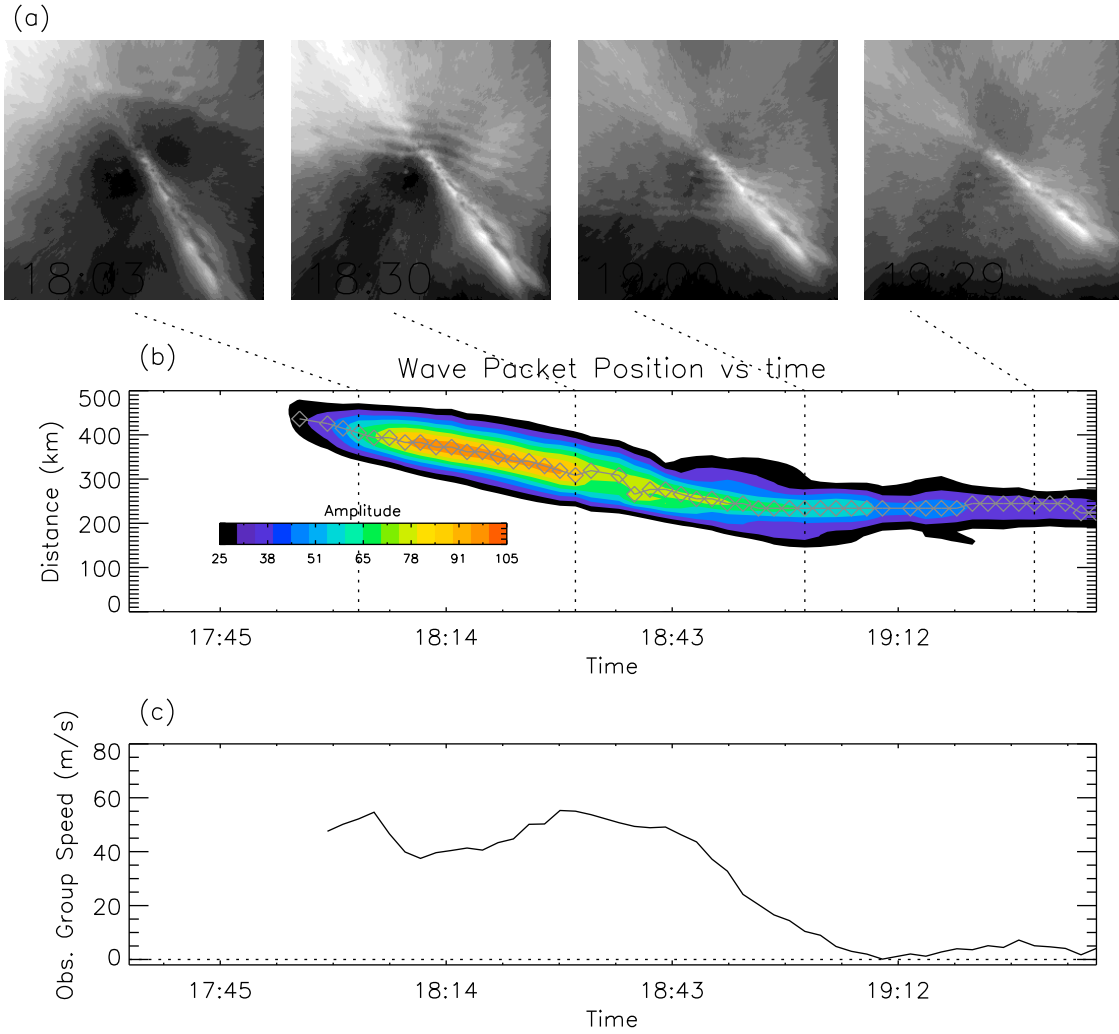
(a)

(b)

(c)

Figure 6. (a) OH images. (b) The position along the y-axis of the amplitude of the bore wave packet as a function of time. The decrease in group velocity and attenuation of the packet's amplitude is apparent. (c) The southward group speed of the bore wave packet.

[2007]. The Cross S-Transform Function ($C[x, y, k_x, k_y, t]$) is defined as

$$C[x, y, k_x, k_y, t_{01}] = S_2[x, y, k_x, k_y, t_1] \cdot S_1[x, y, k_x, k_y, t_0]^* \quad (6)$$

where the * indicates complex conjugate, $t_{01} = (t_0 + t_1)/2$ is an absolutely referenced time stamp, and S_1 and S_2 are the spatial S-Transforms of two space domain series from successive images taken at a time difference of $\Delta t = t_1 - t_0$. One can locate a quasi-monochromatic wave packet as a maximum in the magnitude of the cross ST function at a location $[x_0, y_0, k_{x0}, k_{y0}]$. The phase ϕ of the Cross S-Transform at this point

$$\phi = \arctan\left(\frac{\Im(C[x_0, y_0, k_{x0}, k_{y0}, t_{01}])}{\Re(C[x_0, y_0, k_{x0}, k_{y0}, t_{01}])}\right) \quad (7)$$

indicates the phase shift between the two space domain series over a time Δt. Due to the robust phase properties of the S-transform, the cross ST phase at the local amplitude

maximum is very stable. Knowing the horizontal wavelength λ_h of this quasi-monochromatic wave packet from

$$\frac{1}{|\lambda_h|^2} = |k_{x0}|^2 + |k_{y0}|^2 \quad (8)$$

and noting that the direction of the wavefront is given by the local wave number

$$dir = \arctan\left(\frac{k_{y0}}{k_{x0}}\right) \quad (9)$$

One can infer the observed horizontal phase velocity from equation (7) as

$$V_{ph_{hor}} = \frac{\phi}{2\pi} \cdot \frac{\lambda_h}{\Delta t} \quad (10)$$

where Δt is the time sampling interval between images. One can perform this set of calculations for each point (x, y) from this pair of images.
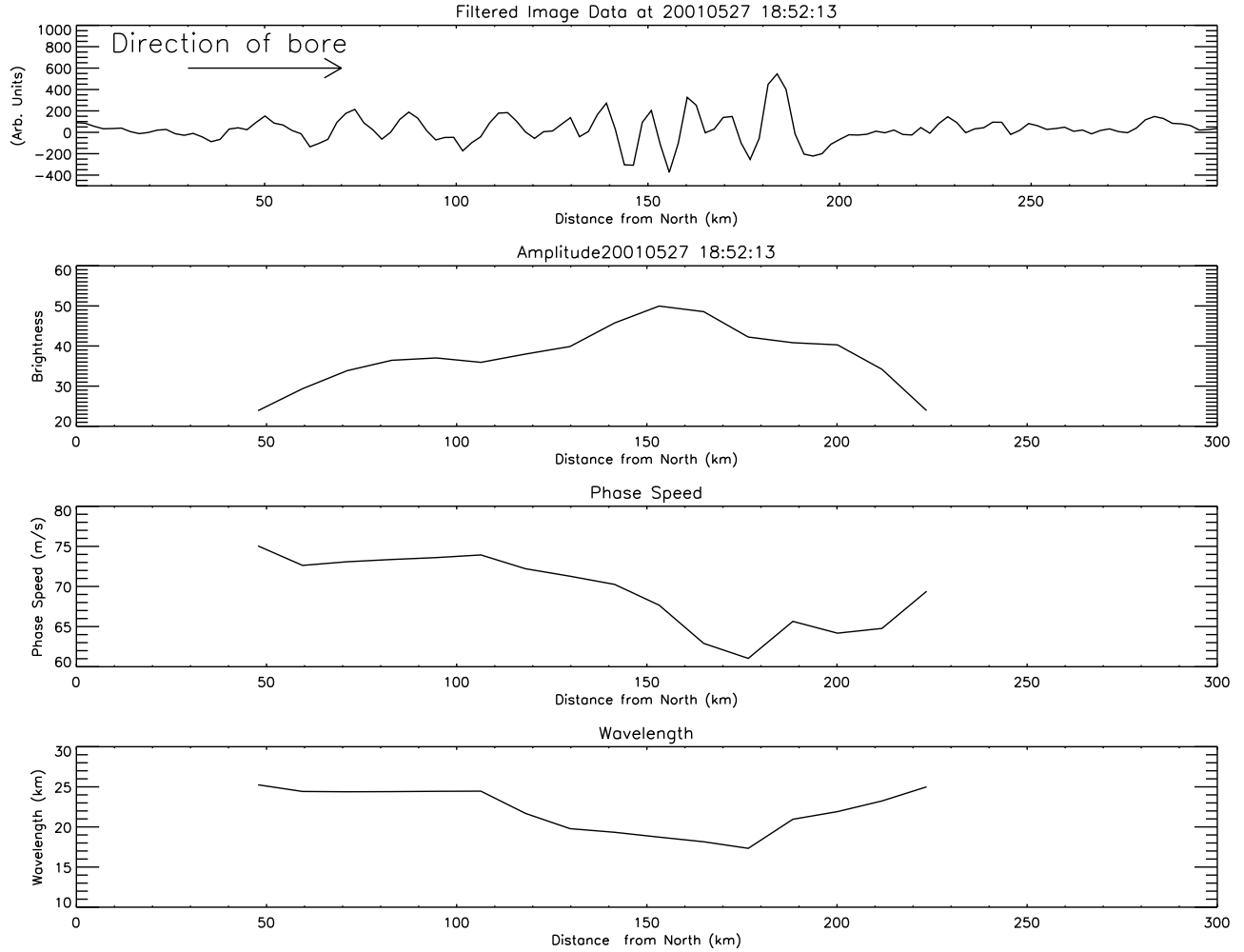
Figure 7. Plot showing the airglow brightness as well as amplitude, phase speed, and wavelength, as a function of distance. The northern edge is at 0 km, and the bore is moving to the right (south). Here the large amplitude waves are moving more slowly. That trend is seen in this analysis for most of the wave train, however the leading edge does have a longer wavelength.

[14] Calculating the (observed) horizontal phase speed of the wave allows one to infer the (observed) frequency and period of the wave based on these two images.

$$T = \frac{1}{f} = \frac{\lambda_h}{|V_{ph_{hor}}|} \qquad (11)$$

3. Measured Parameters of the Bore Wave Packet

[15] In order to isolate strong quasi-monochromatic wave events, the amplitude of the local spatial S-Transform peaks were compared to a threshold amplitude (equal to 25 brightness units). This threshold was based on a statistical analysis of a dark region of the image (i.e. no wave signature). The S-Transform of this region was calculated and these "dark image" amplitudes were determined. Calculations on these dark region results indicated that an S-Transform amplitude of 20 units was at the 99.94% confidence level (i.e. 99.94% of the ST amplitudes of the dark region fell below the threshold of 20 units). A threshold

of 25 units was chosen to be higher than any of the dark S-Transform amplitudes. Based on this analysis, the chance of random fluctuations exceeding this threshold is very small. A large peak in S-Transform amplitude was seen at ≈25 km wavelength which corresponds to the bore wave packet. The position of this peak indicates the peak wave number of the wave packet. In the preprocessed and filtered data set, the bore wave packet was by far the dominant feature in the local amplitude spectrum, allowing us to track the peak spectral amplitude even as it changed its position (i.e. as the position of the amplitude peak wave number of the bore wave packet changed as time progressed or as spatial distance varied.).

3.1. Identification of the Mesospheric Bore

[16] An initial investigation into the bore properties of this event was performed by us in the papers by *Nielsen et al.* [2006] and *Stockwell et al.* [2006]. We have determined in these previous studies that the event exhibited several characteristics consistent with a mesospheric bore event. A single high contrast linear front propagating into the field of
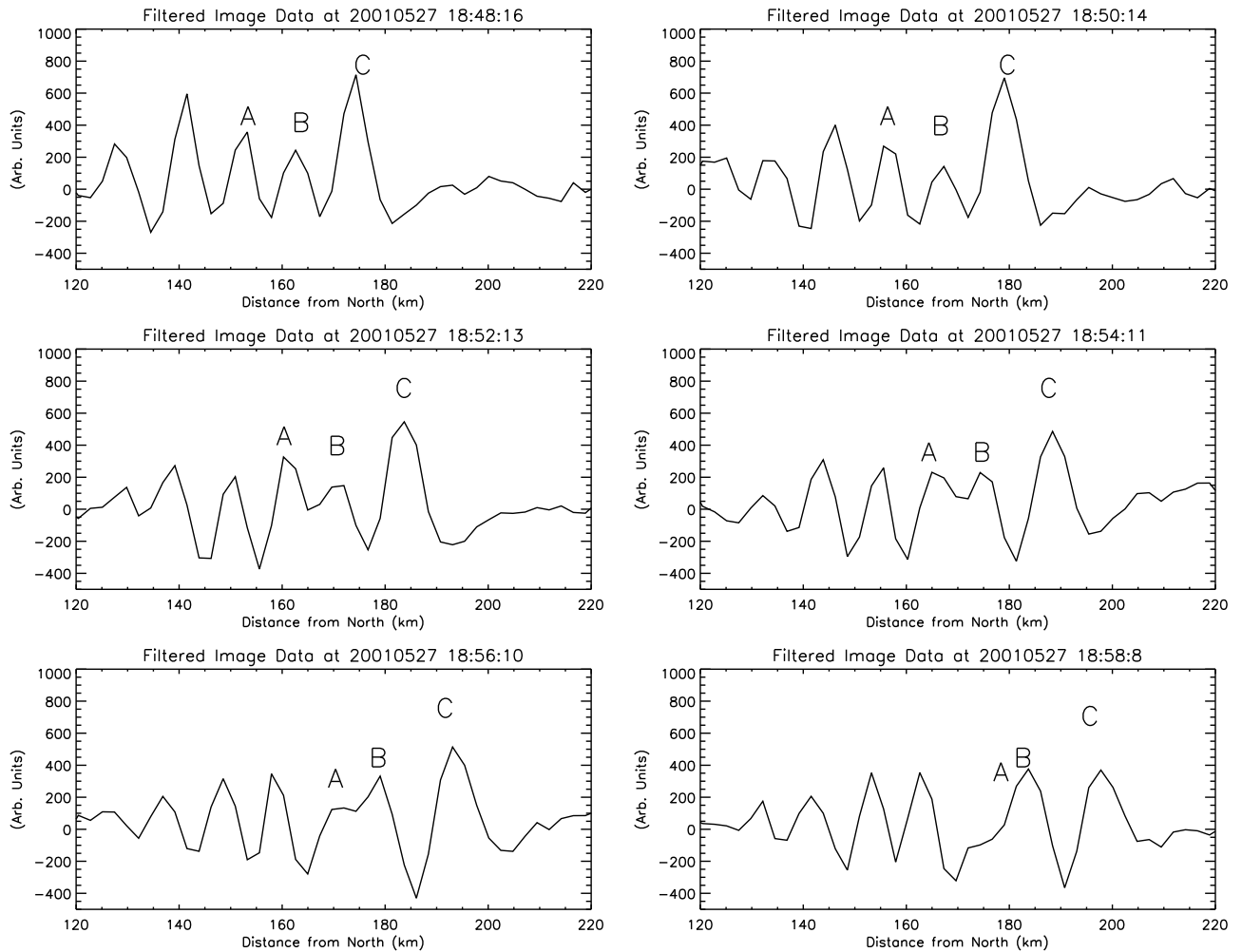
Figure 8. Time series of the filtered image data taken perpendicular to the wavefront (i.e. along y-axis at x = 153 km from north to south) measured as six different times. Wave peaks are labeled C (initial bore wave), B, and A. The phase fronts A and B move at different speeds, and inevitably crash into each other.

view was observed. Sinusoidal waves were observed lagging behind the bore that were being generated in the field of view of the image at a rate of approximately 6.5 waves per hour. This wave has been identified as a mesospheric bore due to the following observations [*Nielsen et al.*, 2006]: (1) the presence of trailing wave crests phase locked to the bore step, (2) step function increase in the airglow emission brightness, and (3) the generation of trailing wave crests observed in the field of view of the imager.

[17] The trailing wave crests can be seen in Figure 1. The bore step is shown in Figure 3. The difference images were averaged over the east-west rows (i.e. parallel to the wavefronts) and are plotted for several different times. The bore step when initially observed has a nearly 30% increase in brightness. However, the low-pass filtering reduces the sharpness of the edge.

3.2. Wavelength

[18] By employing the two dimensional analysis, the full vector nature of the wave packet can be determined, as shown in Figure 4. In addition to being able to calculate

wavelength and the direction of the wavefront, it also can infer these values for all spatial samples of the full 2d image while maintaining the high temporal resolution. Two dimensional analysis can also resolve all types of two dimensional motions such as the rotation of wavefronts. The wavelength vectors are derived from the ST analysis using equations (8) and (9).

[19] As time of night progresses one can see how the wavelength measurements translates southward starting at the north edge (Figure 4). Only results with a local spectral amplitude of greater than the threshold are shown, which effectively describes the bore wave packet. A striking feature of this wave packet's evolution is seen in the observed horizontal wavelength and the observed horizontal phase speed taken from two different times over a 57 minute period. The observed horizontal phase speed decreases from 74 m s^{-1} to 68 m s^{-1}. A possible explanation for this behavior is that the wave packet may have suddenly encountered an increase in horizontal background wind in the direction opposite the wave's propagation. However, during this time the horizontal wavelength decreases from
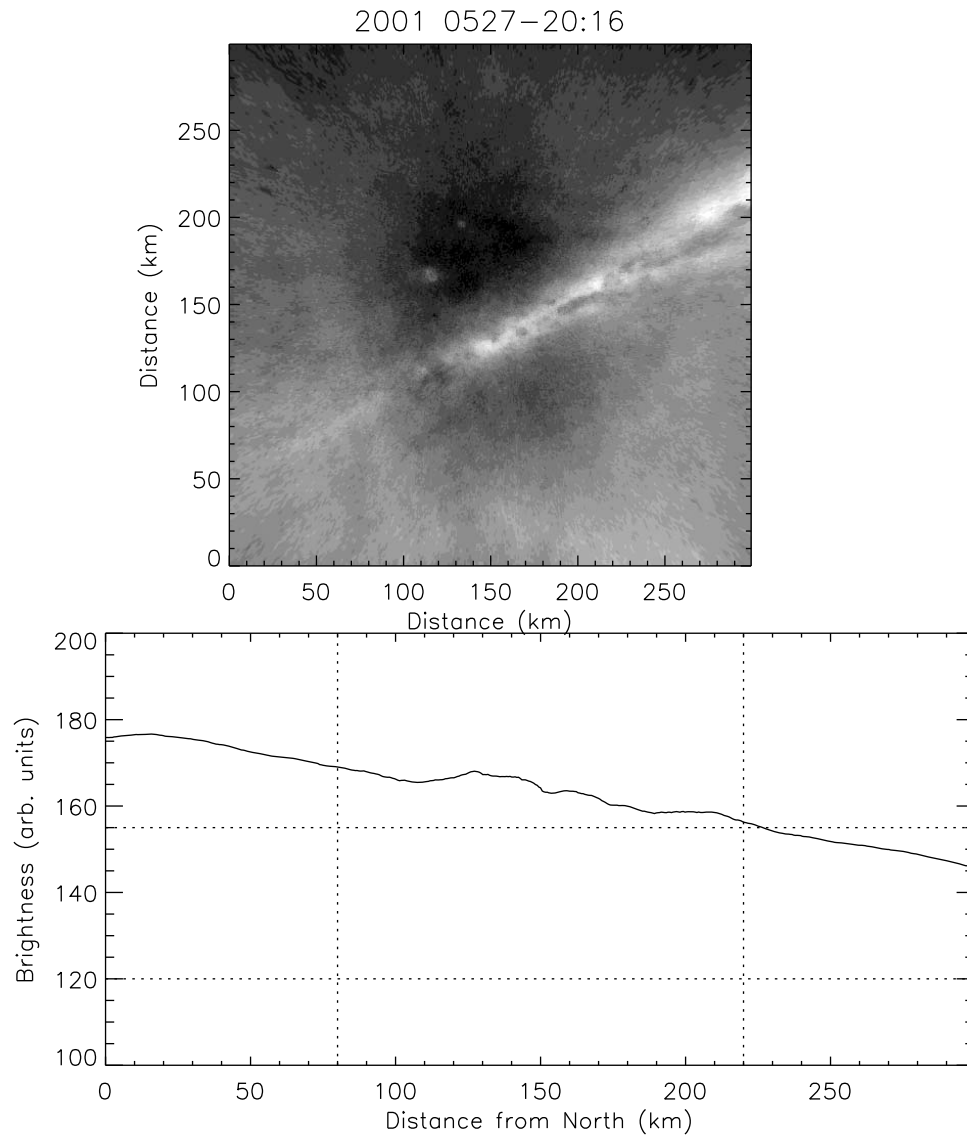
2001 0527−20:16

Figure 9. A plot of the aftermath of the bore event. The top image shows the raw flat fielded image at 20:16 UT. The bottom plot shows the plot of the row average of the low-pass filtered images (Difference Images) where the bore wave has been removed. There is no evidence of the bore step function.

36 km to 22 km, which cannot be explained by the background wind. Additionally, wind profiles indicate that the opposing wind actually accelerates in the direction of the bore propagation (shown below).

3.3. Amplitude

[20] The evolution of the wave packet can be seen in the amplitude of the wave. Figure 5 shows the amplitude given by $|S(x, y, k_{x0}, k_{y0}, t_i)|$ at the same times as Figure 1. The motion of the wave packet in a southward direction (toward the bottom of the images) indicates the group velocity of the wave packet which is consistent with the motion of the brightness step function shown in Figure 3. The group however slows down and stays at position 200 km since approximately 19:00 UT, never reaching the southern edge of the image. Also apparent is the change in the amplitude of the wave, which is quite strong initially (approximately 80 brightness units at 18:1 7UT and 18:26 UT) and is
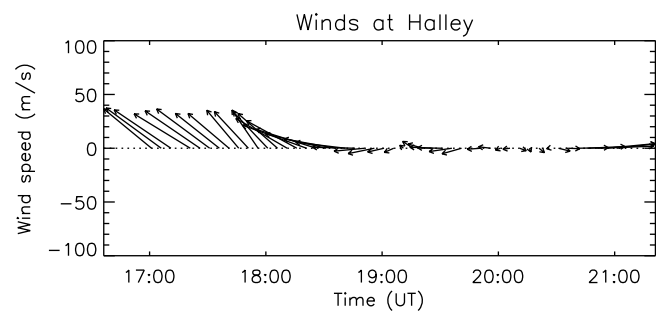

Figure 10. Background winds over Halley Station, Antarctica shown as a vector plot. The measurements were averaged over the OH layer heights (80 km to 95 km) and smoothed in time (15 minutes). There is a strong meridional component of the wind blowing northward early on, and this wind is steadily attenuated to almost a zero wind later.
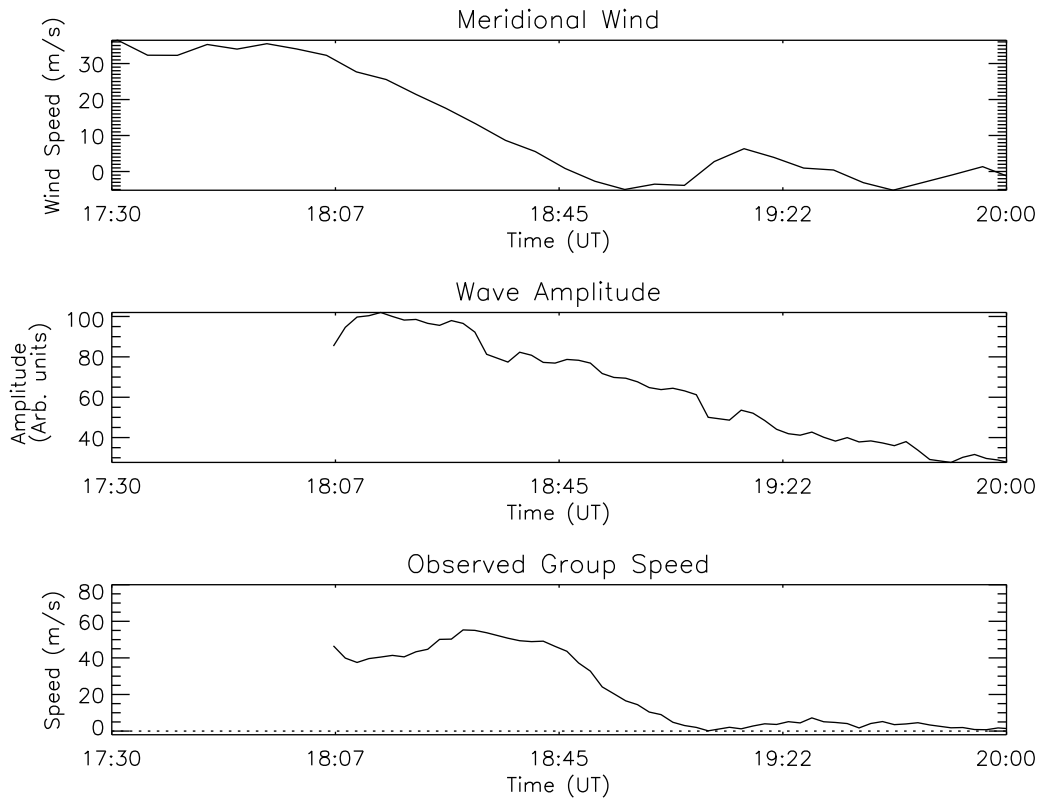
Figure 11. A comparison of the background wind and the ST measured wave packet group speed and amplitude. The meridional wind shows a marked southward acceleration at the same time the bore wave packet has a decelerating southward group speed. Simultaneously the wave packet's amplitude shows a steady attenuation. The start of the wave parameters occur when the wave packet enters the field of the view of the instrument.

steadily attenuated as the wave packet evolves (below approximately 40 brightness units at 19:29 UT).

3.4. Observed Horizontal Group Speed

[21] Since the S-Transform amplitude can localize the wave energy in space for a quasi-monochromatic wave, the amplitude envelope can be tracked over time to measure the position of the wave group throughout the night. Only the southward horizontal component of group velocity can be measured since the width of the wave packet exceeds the field of view of the imager in the east/west direction; if there were group motion parallel to the phase fronts it would not be detectable in these images. The position of the wave group can be seen in Figure 6 where S-Transform amplitudes averaged parallel to the wavefronts ($|S(k_{x0}, y, k_{y0}, t_i)|$, i.e. averaged over the x-axis, east to west, for the image number "i") from many successive images are overplotted. The contours progress southward steadily from $\approx$18:00 UT to $\approx$18:45 UT. After that time, the wave packet's forward motion is stopped, and maintains the same position until $\approx$20:00 UT. The mean peak amplitude position is overplotted (diamonds in Figure 6b) on the contours. The first difference of the wave's group position gives an estimate of the southward group velocity (Figure 6c). The observed horizontal group velocity of the packet slows dramatically, at roughly 18:30 UT. It maintains an approximately zero group velocity after this time.

3.5. Wavelength in the Bore Packet

[22] It is possible to plot the wavelength of the bore wave as a function of distance from the north (top) edge of the image, as shown in Figure 7. A particular snapshot in time is shown, where the measured wave parameters are plotted as a function of distance (a column of the image perpendicular to the wavefronts). The top plot shows the filtered OH intensity along this image column. The front of the bore wave packet is at $\approx$200 km and the wave train extends back to 50 km. The bottom trace shows how the wavelength varies as a function of distance behind the wavefront, with smaller wavelengths in the middle of the bore wave packet. Comparison with the second plot of Figure 7 shows that the minimum wavelength occurs at the maximum amplitude. However, the overall trend is for wavelengths to increase with distance from the bore step as expected, as seen from distance 180 km to 50 km. The leading peak is the largest, but the following two peaks are smaller. The ST amplitude response has a spatial resolution corresponding to the wavelength of the signal, thus the strongest coherent amplitude response occurs in the middle of the wave packet at a distance of 150 km.

3.6. Amplitude Versus Phase Speed

[23] Observations of amplitude ordering of the wave train have been made in the literature [*Smith et al.*, 2003;
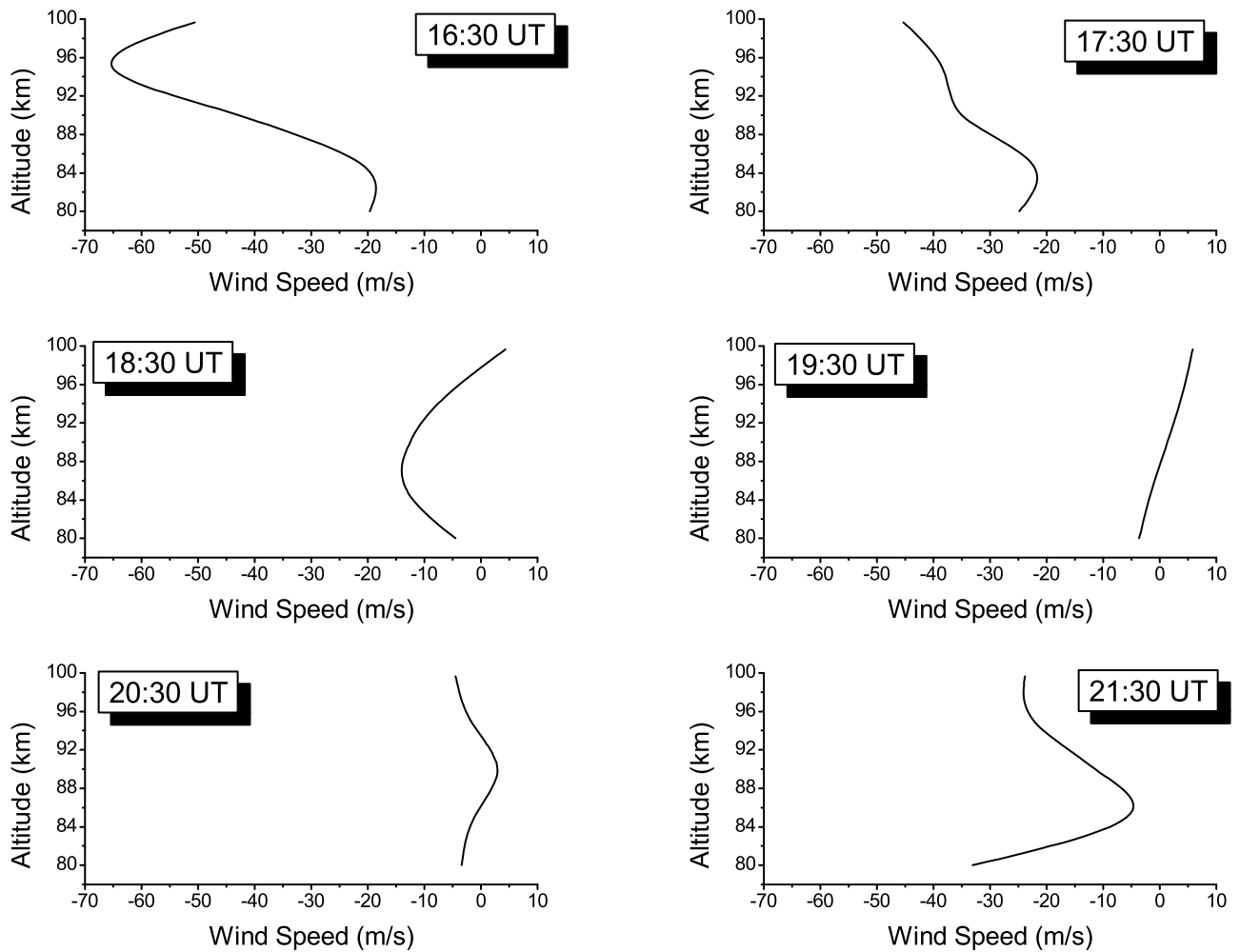
Figure 12. Hourly averaged wind speed in the direction of wave propagation obtained from the IDI instrument located at Halley Station. The wave moves into a strong headwind (17:30 UT) and as the wave progressed overhead of Halley Station the background wind decreases significantly to near 0 m s^{-1}.

Mahapatra et al., 1991] where the leading wavefronts have the largest amplitudes, and these leading wavefronts are moving faster than smaller amplitude trailing wavefronts. The velocity and amplitude ordering of the wavefronts has also been shown analytically [*Christie*, 1989].

[24] Here the opposite effect can be observed, large amplitude wave crests are seen to travel more slowly than the smaller amplitude wave crests (Figure 7). The front of the bore is at ≈200 km (but not shown in this filtered data). The amplitude peaks in the middle of the bore wave packet which corresponds to the lowest wavelength and also the lower phase speeds.

3.7. Wavefront Collision

[25] Upon examination of the phase speed plots of the bore wave, an interesting situation arises. The fact that this wave packet has different phase speeds (dispersive) implies that the phase fronts of this wave packet will eventually collide with each other. That is indeed what happens as is shown in Figure 8.

[26] These plots show the filtered image data taken along the y-axis (from north to south) perpendicular to the wavefront from the middle of the image (x = 153 km) for eight consecutive images with a 2 minute time step. As one looks at the phase velocity as a function of southward distance (Figure 7), a small dip can be seen in phase speed, indicating that for that particular region of the wave, the leading phase fronts should be moving slower than the following phase fronts. In Figure 8, one can see that this is indeed the case, as the following wavefronts (labeled A) have caught up and are combining with the leading phase fronts (labeled B). The next several plots show the further evolution of these wavefronts as they combine; as peak A and peak B get close and eventually merge. Additionally, the amplitude ordering changes. Initially, B < A and A < trailing wave crest (Figure 8). In the final frame, we have a more natural amplitude ordering, with the larger amplitudes leading.

3.8. Aftermath of the Bore Event

[27] The state of the OH layer after the bore event is shown in Figure 9. The Milky Way dominates the image. In the bottom plot, the OH brightness, averaged along the wave crests, is shown. There is no evidence of the remnants
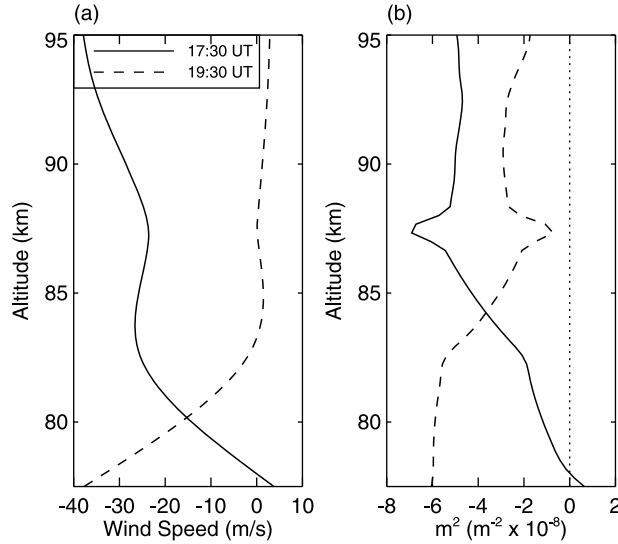
Figure 13. Vertical profiles of (a) the wind speed and (b) the vertical wave number squared (m^{-2}) for 17:30 UT (solid line) and 19:30 UT (dashed line). Negative values indicate a Doppler ducted or evanescent wave. At 17:30 UT there freely propagating region at the lowest altitude below 78 km with an evanescent region existing above 78 km. Later at 19:30 UT it is purely evanescent over the entire region region (from 75 km to 95 km) and shows no sign of a possible Doppler duct.

of the bore step (compare to Figure 3) only a smooth decrease in brightness toward the southern edge, with a much lower slope ($\approx$0.1 units/km) than what is seen in Figure 3 ($\approx$0.5 units/km).

4. State of the Atmosphere

[28] As a wave packet propagates into a region of non-zero horizontal wind, the effect of the background wind results in a Doppler shift in the observed quantities. The intrinsic horizontal wavelength is equal to the observed horizontal wavelength, but observed phase velocity, observed group velocity, observed period will not necessarily be equal to their intrinsic counterparts.

$$c_{p_{obs}} = c_p + U_b \quad (12)$$

$$c_{g_{obs}} = c_g + U_b \quad (13)$$

where U_b is the background wind in the direction of wave motion. In addition, the propagation of the characteristic bore wall would also be affected by the background wind

$$c_{wall_{obs}} = c_{wall} + U_b \quad (14)$$

As the wave packet propagates into a region of opposing horizontal wind, the observed phase and group velocity decrease, and the observed period will increase (such that the wavelength $\lambda = c_{p_{obs}} T$ will remain constant).

[29] A vector time series of the background winds from the BAS Imaging Doppler Interferometer is shown in Figure 10. This shows the vector plot (top is north, east is to the right) of the horizontal winds averaged from 80 to 95 km, and smoothed in time with a 15 minute window. There is a strong wind blowing from 16:45UT until $\approx$18:30 UT after which is it observed to diminish. There is a large decrease in the meridional wind from 18:00UT to 19:00 UT, where the $\approx$35 m s^{-1} northward wind decreases to approximately zero, indicating a very strong southward acceleration (i.e. in the direction of wave propagation) of 990 m s^{-1}/day.

[30] In Figure 11 the meridional wind is shown with the bore wave amplitude and horizontal group velocity. The acceleration of the meridional wind roughly coincides with the deceleration of the bore wave packet and also with the decrease in the amplitude of the bore wave.

4.1. Vertical Profile of m^2

[31] The IDI wind profiles used to produce Figure 10 are shown in Figure 12. They can be used to investigate the propagation nature of the wavefield; if the wave is freely propagating, Doppler ducted or evanescent. A wave is freely propagating if the vertical wave number is real. The vertical wave number can be calculated using [Nappo, 2002]:

$$m^2 = \frac{N^2}{(c - U_b)^2} + \frac{U_b''}{(c - U_b)} - \frac{1}{H}\frac{U_b'}{(c - U_b)} - \frac{1}{4H^2} - k^2 \quad (15)$$

where c is the horizontal phase velocity of the wave, U_b is the background wind and k is the horizontal wave number. The wave numbers here include a factor of 2π. The scale height H and the Brunt-Vaisala frequency N, were estimated using MSIS model temperature and the following equations:

$$H = \frac{RT}{g} \quad (16)$$

$$N^2 = \frac{g}{T}\left(\frac{dT}{dz} + \Gamma\right) \quad (17)$$

where g = 9.65 m s^{-2}, Γ = 9.5 K/km and R is the gas constant.

[32] Using hourly averaged wind measurements and the average observed wave parameters, the vertical wave number was calculated using the above equation. Figure 13b shows the vertical wave number squared (m^2) as a function of altitude at two times during the wave event. At 17:30 a freely propagating region exists below 78 km with an evanescent region existing above 78 km. The next three hours the airglow region (80–95 km) maintains a pure evanescent region and shows no sign of a possible Doppler duct. The existence of a thermal duct as discussed by Dewan and Picard [1998] and Laughman et al. [2009] cannot be investigated as no temperature data are available.

4.2. Comparison with Bore Theory

[33] Dewan and Picard [1998] outlined the basic theory for mesospheric bores, calculating relationships between the undisturbed vertical depth or thickness of the duct h_0, and increased duct thickness h_1 due to the jump after the bore,
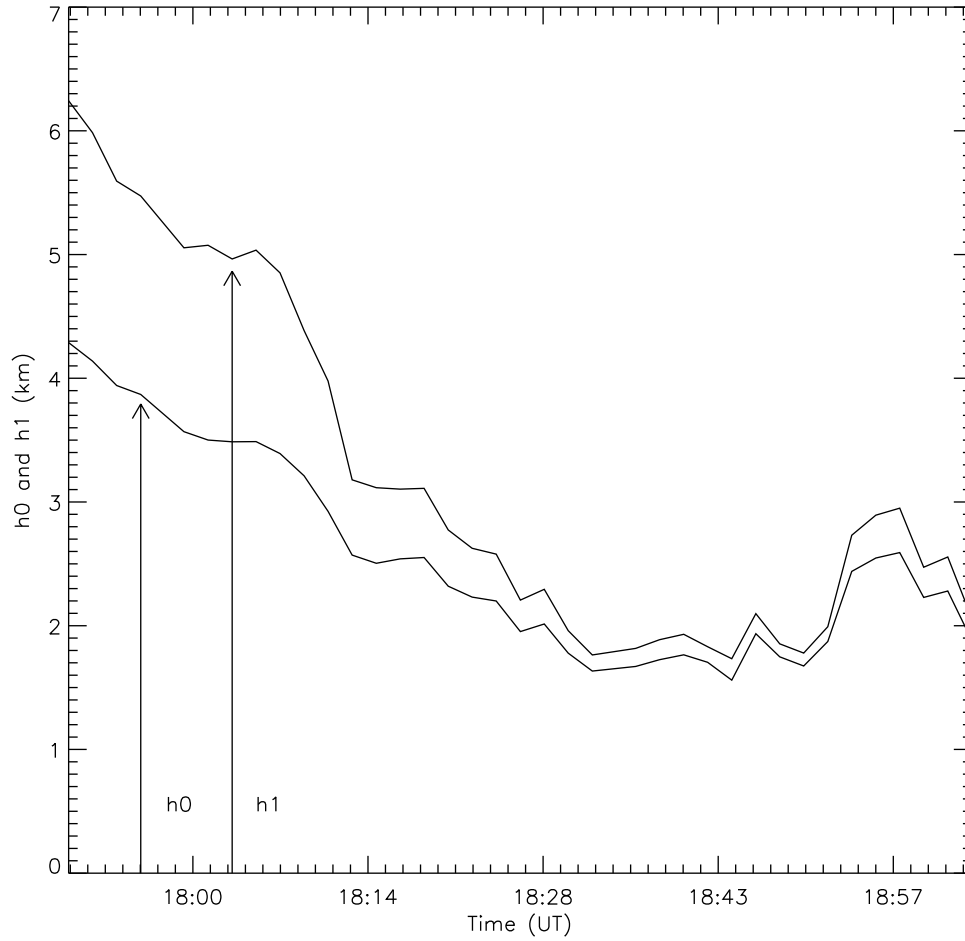
Figure 14. Plot of the calculated values for h_0 and h_1. Over the evolution of the bore wave, the duct is decreasing dramatically. Linear interpolation was used through the missing data gaps due to instrument calibration.

and propagation speed, horizontal wavelength, and wave amplitude. These results are summarized here:

$$U_0 = \sqrt{g' \frac{h_1(h_1 + h_0)}{2h_0}} \qquad (18)$$

$$\lambda_h = \frac{2\pi h_1}{3} \sqrt{\frac{2h_0}{h_1 - h_0}} \qquad (19)$$

$$a = \frac{1}{\sqrt{3}} \frac{h_1(h_1 - h_0)}{h_0} \qquad (20)$$

where U_0 is the bore speed, λ_h is the wavelength, g' is the acceleration due to gravity corrected for buoyancy, and a is the wave amplitude.

[34] For our calculations, the value $g' = 1.4$ ms^{-1} from *Dewan and Picard* [1998] is used. By definition, h_1 is always greater than h_0. These equations assume a zero background wind. For all of our calculations, we have removed the background wind from the observed wave variables.

[35] By calculating the first derivative of the wavelength function, the local minimum for bore wavelength as a function of the bore jump height can be found analytically at

$$h_1 = 2h_0 \qquad (21)$$

and also trivially at $h_1 = 0$ which is a non-physical solution since h_1 must always be greater than h_0. Because of this minimum in the calculated bore wavelength, it may be possible to resolve a consistent pair of h_0 and h_1 values that can account for the observations. The observed horizontal wavelength of approximately 20 km has implications for the maximum value of the duct depth.

[36] The bore theory equations for bore wavelength λ_h and bore speed U_0 both depend on h_0 and h_1. Knowing the wavelength and speed from the airglow measurements, this reduces to two equations in two unknowns and can be solved leading to the following dependence of bore duct depth h_0 on the bore jump height h_1

$$h_0 = \frac{g' h_1^2}{2U_0^2 - g' h_1} \qquad (22)$$

and a fourth order polynomial equation in the bore jump height h_1

$$\left(\frac{2\pi}{3}\right)^2 g' h_1^4 + \lambda_h^2 g' h_1^2 - \lambda_h^2 U_0^2 h_1 = 0 \qquad (23)$$
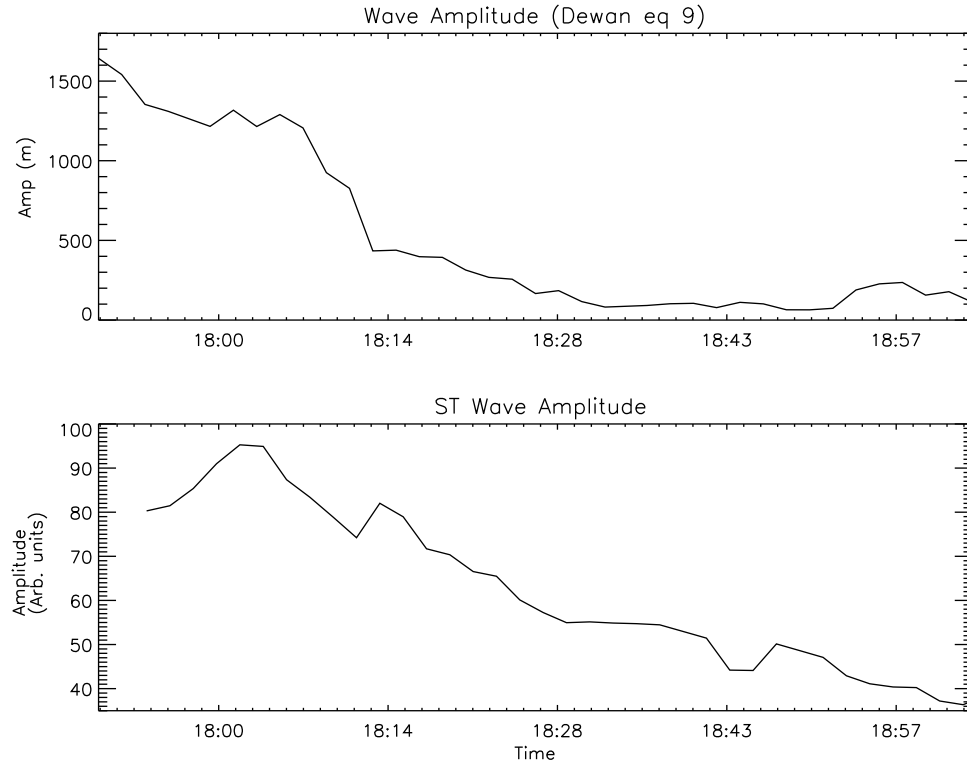
Figure 15. Comparison of theoretical predictions and observed parameters. Top plot shows the calculate values for the wave amplitude from Dewan and Picard (equation (9)). The bottom plot shows the measured S-Transform amplitude of the bore wave in arbitrary OH brightness units. While there is no relationship between the units of a and ST amplitude, there is good agreement between the two traces as the bore evolves.

This has a trivial yet non-physical solution of $h_1 = 0$, and the other three solutions can be solved by use of a cubic equation solver. For typical values of U_0 and λ_h measured from this bore event, there is one real-valued solution, and two complex solutions.

[37] Calculations for h_0 and h_1 are made for each set of images, and plotted in Figure 14. Points where calibration breaks led to a loss of data were linearly interpolated.

[38] With the values of h_0 and h_1, one can calculate the bore wave amplitude a [meters or kilometers] and the normalized bore strength β [dimensionless], and thus we can write the wave amplitude a in terms of the observable values U_0 and λ_h (see Appendix A). This allows us to perform a direction comparison between the predictive values for $a(\lambda_h, U_0)$, and the measured ST amplitude of the bore wave shown in Figure 15. Here, the top plot shows the calculated
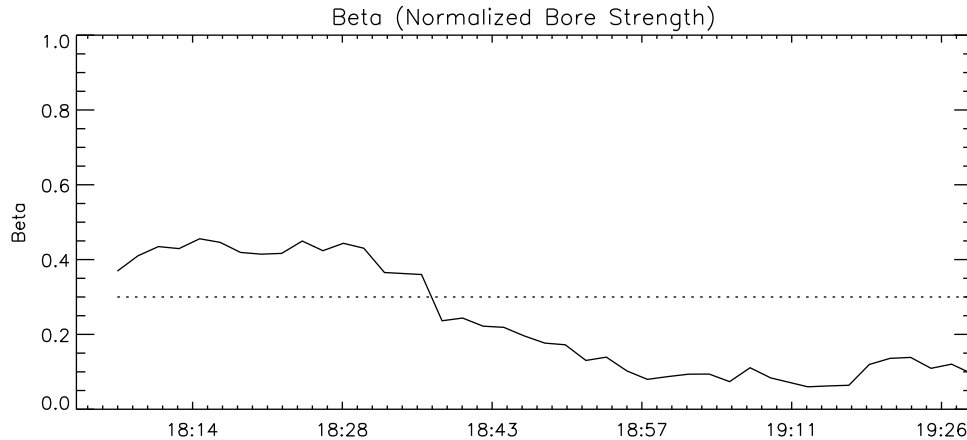

Figure 16. Calculation of the normalized bore strength as a function of time of night. The dotted line indicates a value equal to 0.3. If a bore wave exceeds this threshold, then it should become turbulent.

values (using equation (20)) for the wave amplitude. The bottom plot shows the measured S-Transform amplitude of the bore wave in arbitrary OH brightness units. While there is no relationship between the units of a (km) and ST amplitude (arbitrary brightness units), the agreement of the two traces as the bore event evolves is good.

[39] One can also calculate the normalized bore strength from these values for h_0 and h_1 using

$$\beta = \frac{h_1 - h_0}{h_0} <= 0.3 \qquad (24)$$

where $\beta = 0.3$ is approximately the maximum value for an undular bore. If the normalized bore strength exceeds a value of 0.3, then the bore will become turbulent [*Dewan and Picard*, 1998]. As can be seen in Figure 16, the normalized bore strength is initially very large, exceeding the breaking threshold by ≈50%. This indicates that the bore should become turbulent. Later, the value for β steadily declines from 18:30 to 19:00 and levels off to a very weak 0.1 after 19:00 UT as the bore dissipates.

5. Conclusion

[40] There has been much work on wave breaking scenarios in the middle atmosphere, both theoretical/modeling [*Andreassen et al.*, 1994; *Fritts et al.*, 1997] and observational [*Fritts et al.*, 1993; *Hecht et al.*, 1997]. *Taylor and Hapgood* [1990] suggested that small scale ripples seen in airglow observations are the results of dynamical instabilities. *Fritts et al.* [1993] observed characteristic band and streak structures in noctilucent clouds. They described enhanced brightness along a discreet phase of the incident wave motion, and brightness streaks that aligned perpendicular to the bright phase structure. *Hecht et al.* [1997], as part of the CORN campaign, observed small horizontal structures that appeared perpendicular to propagating 30–50 km wavelength gravity waves in OH airglow. In a companion paper, *Fritts et al.* [1997] also employed a 3D model that predicted small-scale (5 to 10 km) ripple pattern aligned perpendicular to the phase fronts. Had a wave breaking mechanism been the reason for the observation that the wave packet slowed down and disappeared, one would expect to see these ripple patterns. However, none were observed. Instead we observe a strong wave packet quickly dissipate with no ripple signature.

[41] The physical system in which this mesospheric bore wave packet propagated is different than the situation described in these papers for the wave breaking signatures. In this case there is evidence that the wave is ducted, and the duct in which it is propagating collapses and no longer capable of sustaining the bore wave.

[42] The observations here, by use of local spectral analysis techniques, gives a more quantitative measure of wave breaking characteristics than the signature structures described above. The large bore wave event is fully characterized by S-Transform analysis. Only two images are required to calculate a single estimate of phase velocity, group velocity, and period. In this data set, the evolution of a large bore step function with a trailing phase locked wave train was observed. As the wave packet progressed into the field of view, several key parameters of the wave packet underwent a significant change. The horizontal phase speed

decreased, associated with a corresponding decrease in horizontal wavelength. Simultaneously with these results, the movement of the wave group was seen to decelerate and come to a halt as the wave packet's amplitude attenuated. The bore step dissipated, having never reached the south edge of the field of view. This presents strong circumstantial evidence of a dissipating wave event. The phase speed and wavelength results, when applied to bore theory, indicates the presence of a bore duct and the gradual collapse of this duct. The opposite of expected amplitude ordering of the wave crests was observed, at times trailing crests had a larger amplitude than leading crests. Also, the opposite of the expected velocity ordering was seen, as trailing waves traveled faster than leading crests, resulting in the wave crest pileup which may be indicative of an instability or wave breaking mechanism that occurs in this type of situation.

[43] There are several caveats that bear mentioning: i) the meridional wind decrease appears to start a bit before the wave appears; ii) the zonal wind also changes throughout this whole event (as seen in Figure 10) but to a much smaller degree; iii) there is no direct evidence that a) there was a duct, or b) that the duct collapsed. That is entirely based on the observation of wavelength and phase speed derived from the airglow images.

[44] Even given these caveats, a plausible explanation of the events observed on this night is that the bore wave packet, possibly traveling along a thermal duct, encountered a region where the duct collapsed. The wave evolves (U and λ decrease), slows down (horizontal group velocity decreases to zero) and the amplitude attenuates while the background wind showed a large acceleration in the direction of the wave propagation (indicating momentum deposition from the breaking bore, though we note that this is merely a coincident observation and we have no evidence of a causal relationship between the wave and the background wind). *Dewan and Picard*'s equations were applied and it is seen that the bore duct depth decreased to a negligible depth during this time. The direct observation of the wave amplitude was measured with the ST analysis, and compared to the predicted values for a bore wave amplitude from Dewan and Picard, and showed very good agreement. If this is indeed a record of the breaking of a ducting wave resulting in an acceleration of the mean flow, which would have a significant impact on the understanding of mesosphere/lower thermosphere dynamics.

Appendix A: Derivation of Bore Parameters as a Function of Airglow Measurements

[45] *Dewan and Picard* [1998] provided three equations relating the bore speed, horizontal wavelength and wave amplitude (equations (18), (19), (20)) as a function of h_0 and h_1. From equations (18) and (19), we obtain equations (A1) and (A2).

$$h_0 = \frac{g' h_1^2}{2U_0^2 - g' h_1} \qquad (A1)$$

$$h_0 = \frac{\lambda_h^2 h_1}{\lambda_h^2 + 2\left(\frac{2\pi}{3}\right)^2 h_1^2} \qquad (A2)$$

Equating these two leads to equation (23) which can be rewritten in the form:

$$h_1^3 + Ah_1 + B = 0 \tag{A3}$$

where

$$A = \frac{\lambda_h^2}{\left(\frac{2\pi}{3}\right)^2} \tag{A4}$$

and

$$B = -\frac{\lambda_h^2 U_0^2}{\left(\frac{2\pi}{3}\right)^2 g'} \tag{A5}$$

The solution of this cubic equation (A3) depends on the sign of the discriminant D:

$$D = \frac{A^3}{24} + \frac{B^2}{4} \tag{A6}$$

Here, A is always positive, and therefore $D > 0$ and this equation has one real root and two imaginary roots. The real root is given by

$$h_1 = \left(-\frac{B}{2} + \sqrt{D}\right)^{1/3} + \left(-\frac{B}{2} - \sqrt{D}\right)^{1/3} \tag{A7}$$

therefore

$$h_1(U_0, \lambda_h) = \left[\frac{\lambda_h^2 U_0^2}{2\left(\frac{2\pi}{3}\right)^2 g'} + \frac{\lambda_h^2}{2\left(\frac{2\pi}{3}\right)^2}\left(\frac{\lambda_h^2}{6\left(\frac{2\pi}{3}\right)^2} + \frac{U_0^4}{g'^2}\right)^{1/2}\right]^{1/3}$$
$$+ \left[\frac{\lambda_h^2 U_0^2}{2\left(\frac{2\pi}{3}\right)^2 g'} - \frac{\lambda_h^2}{2\left(\frac{2\pi}{3}\right)^2}\left(\frac{\lambda_h^2}{6\left(\frac{2\pi}{3}\right)^2} + \frac{U_0^4}{g'^2}\right)^{1/2}\right]^{1/3} \tag{A8}$$

Now one can substitute equation (A1) into equation (20) and rearrange to get

$$a = \frac{2}{\sqrt{3}}\left[\frac{U_0^2}{g'} - h_1\right] \tag{A9}$$

which leads to

$$a(U_0, \lambda_h)$$
$$= \frac{2}{\sqrt{3}}\left(\frac{U_0^2}{g'} - \left[\frac{\lambda_h^2 U_0^2}{2\left(\frac{2\pi}{3}\right)^2 g'} + \frac{\lambda_h^2}{2\left(\frac{2\pi}{3}\right)^2}\left(\frac{\lambda_h^2}{6\left(\frac{2\pi}{3}\right)^2} + \frac{U_0^4}{g'^2}\right)^{1/2}\right]^{1/3}\right.$$
$$\left. - \left[\frac{\lambda_h^2 U_0^2}{2\left(\frac{2\pi}{3}\right)^2 g'} - \frac{\lambda_h^2}{2\left(\frac{2\pi}{3}\right)^2}\left(\frac{\lambda_h^2}{6\left(\frac{2\pi}{3}\right)^2} + \frac{U_0^4}{g'^2}\right)^{1/2}\right]^{1/3}\right) \tag{A10}$$

This is the "wave amplitude" plotted in Figure 15, and compared to the direct ST amplitude measured from the airglow images.

References

Andreassen, Ø., C. E. Wasberg, D. C. Fritts, and J. R. Isler (1994), Gravity wave breaking in two and three dimensions: 1. Model description and comparison of two-dimensional evolutions, *J. Geophys. Res.*, *99*(D4), 8095–8108, doi:10.1029/93JD03435.

Batista, P. P., B. R. Clemesha, D. M. Simonich, M. J. Taylor, H. Takahashi, D. Gobbi, I. S. Batista, R. A. Buriti, and A. F. Medeiros (2002), Simultaneous lidar observation of a sporadic sodium layer, a "wall" event in the OH and OI 5577 airglow images and the meteor winds, *J. Atmos. Sol. Terr. Phys.*, *64*, 1327–1335.

Brigham, E. O. (1974), *The Fast Fourier Transform*, Prentice-Hall, Englewood Cliffs, N. J.

Brown, L. B., A. J. Gerrard, J. W. Meriwether, and J. J. Makela (2004), All-sky imaging observations of mesospheric fronts in OI 557.7 nm and broadband OH airglow emissions: Analysis of frontal structure, atmospheric background conditions, and potential sourcing mechanisms, *J. Geophys. Res.*, *109*, D19104, doi:10.1029/2003JD004223.

Christie, D. R. (1989), Long nonlinear waves in the lower atmosphere, *J. Atmos. Sci.*, *46*(11), 1462–1491.

Dewan, E. M., and R. H. Picard (1998), Mesospheric bores, *J. Geophys. Res.*, *103*(D6), 6295–6305.

Fechine, J., C. M. Wrasse, H. Takahashi, A. F. Medeiros, P. P. Batista, B. R. Clemesha, L. M. Lima, D. C. Fritts, B. Laughman, M. J. Taylor, P. D. Paulet, M. G. Mlynczak, and J. M. Russell (2009), First observation of an undular mesospheric bore in a Doppler duct, *Ann. Geophys.*, *27*, 1399–1406.

Fritts, D. C., J. R. Isler, G. E. Thomas, and Ø. Andreassen (1993), Wave breaking signatures in noctilucent clouds, *Geophys. Res. Lett.*, *20*, 2039–2042.

Fritts, D. C, J. R. Isler, J. H. Hecht, R. L. Walterscheid, and Ø. Andreassen (1997), Wave breaking signatures in sodium densities and OH nightglow: 2. Simulation of wave and instability structures, *J. Geophys. Res.*, *102*(D6), 6669–6684.

Hecht, J. H., R. L. Walterscheid, D. C. Fritts, J. R. Isler, D. C. Senft, C. Gardner, and S. Franke (1997), Wave breaking signatures in OH airglow and sodium densities and temperatures: 1. Airglow imaging, Na lidar, and MF radar observations, *J. Geophys. Res.*, *102*(D6), 6655–6668, doi:10.1029/96JD02619.

Laughman, B., D. C. Fritts, and J. Werne (2009), Numerical simulation of bore generation and morphology in thermal and Doppler ducts, *Ann. Geophys.*, *27*, 511–523.

Mahapatra, P. R., R. J. Doviak, and D. S. Zrni (1991), Multisensor observation of an atmospheric undular bore, *Bull. Am. Meteorol. Soc.*, *72*, 1468–1480.

Mansinha, L., R. G. Stockwell, and R. P. Lowe (1997), Pattern analysis with two dimensional spectral localization: Applications of two dimensional S Transforms, *Physica A*, *239*, 286–295.

Medeiros, A. F., J. Fechine, R. A. Buriti, H. Takahashi, C. M. Wrasse, and D. Gobbi (2005), Response of OH, O2 and OI 5577 airglow emissions to the mesospheric bore in the equatorial region of Brazil, *Adv. Space Res.*, *35*(11), 1971–1975.

Nappo, C. J. (2002), *An Introduction to Atmospheric Gravity Waves*, Academic, New York.

Nielsen, K., M. J. Taylor, R. G. Stockwell, and M. J. Jarvis (2006), An unusual mesospheric bore event observed at high latitudes over Antarctica, *Geophys. Res. Lett.*, *33*, L07803, doi:10.1029/2005GL025649.

Seyler, C. E. (2005), Internal waves and undular bores in mesospheric inversion layers, *J. Geophys. Res.*, *110*, D09S05, doi:10.1029/2004JD004685.

She, C. Y., T. Li, B. P. Williams, T. Yuan, and R. H. Picard (2004), Concurrent OH imager and sodium temperature/wind lidar observation of a mesopause region undular bore event over Fort Collins/Platteville, Colorado, *J. Geophys. Res.*, *109*, D22107, doi:10.1029/2004JD004742.

Shiokawa, K., S. Suzuki, Y. Otsuka, T. Ogawa, T. Nakamura, M. G. Mlynczak, and J. M. Russell III (2006), A multi-instrument measurement of a mesospheric front-like structure at the equator, *J. Meteorol. Soc. Jpn.*, *84*, 305–316.

Smith, S. M., M. J. Taylor, G. R. Swenson, C.-Y. She, W. Hocking, J. Baumgardner, and M. Mendillo (2003), A multidiagnostic investigation of the mesospheric bore phenomenon, *J. Geophys. Res.*, *108*(A2), 1083, doi:10.1029/2002JA009500.

Smith, S. M., J. P. Friedman, S. Raizada, C. Tepley, J. Baumgardner, and M. Mendillo (2005), Evidence of mesospheric bore formation from a breaking gravity wave event: simultaneous imaging and lidar measurements, *J. Atmos. Sol. Terr. Phys.*, *67*(4), 345–356, doi:10.1016/j.jastp.2004.11.008.

Stockwell, R. G. (2007) Why use the S-Transform?, in *Pseudo-Differential Operators: Partial Differential Equations and Time-Frequency Analysis*, *Fields Inst. Comm.*, vol. 52, edited by L. Rodino, B.-W. Schulze, and M. W. Wong, pp. 279–310, Fields Inst. for Res. in Math. Sci., Toronto, Ont., Canada.

Stockwell, R. G., M. J. Taylor, K. Nielsen, and M. J. Jarvis (2006), A novel joint space-wavenumber analysis of an unusual Antarctic gravity wave event, *Geophys. Res. Lett.*, *33*, L08805, doi:10.1029/2005GL025660.

Taylor, M. J., and M. A. Hapgood (1990), On the origin of ripple-type structure in the OH nightglow emission, *Planet. Space Sci.*, *38*, 1421–1430.

Taylor, M. J., D. Turnbull, and R. P. Lowe (1995), Spectrometric and imaging measurements of a spectacular gravity-wave event observed during the Aloha-93 campaign, *Geophys. Res. Lett.*, *22*(20), 2849–2852.

Yue, J., C. She, T. Nakamura, S. Harrell, and T. Yuan (2010), Mesospheric bore formation from large-scale gravity wave perturbations observed by collocated all-sky OH imager and sodium lidar, *J. Atmos. Sol. Terr. Phys.*, *72*(1), 7–18.

M. J. Jarvis, British Antarctic Survey, Madingley Road, Cambridge CB3 0ET, UK.

K. Nielsen and M. J. Taylor, Center for Atmospheric and Space Sciences, Utah State University, 4405 Old Main Hill, Logan, UT 84322-4405, USA.

R. G. Stockwell, Colorado Research Associates, 3381 Mitchell Ln., Boulder, CO 80301, USA. (stockwell@co-ra.com)